Journal of Computer Science and Technology Studies
ISSN: 2709-104X
DOI: 10.32996/jcsts
Journal Homepage: www.al-kindipublisher.com/index.php/jcsts

JCSTS
AL-KINDI CENTER FOR RESEARCH AND DEVELOPMENT

| RESEARCH ARTICLE

Surface Plasmon Lasers: Quantum Dot

Khalifa Ahmed Salama
Libyan Center for Engineering Research and Information Technology, Libya
Corresponding Author: Khalifa Ahmed, **E-mail**: ka5677675@gmail.com

| ABSTRACT
A surface plasmon laser incorporates a metal layer, an additional medium layer given on the metal layer, and a round structure segment in which a murmuring exhibition mode is created in which surface plasmon light is produced because of surface plasmon reverberation on a connection point with the metal layer pivots along a circle, and a twisted piece framed to yield a piece of laser light created in the round structure part of the addition medium layer. We consider a thin layer of an n-type semiconductor sandwiched between a metal and a p-type semiconductor, and the p-n intersection is forward-one-sided. The mode design of the SPW, engendering along the metal surface, stretches out up to the p-n intersection, where it incites electron-opening recombination and gets intensified. The optical increase of the SPW laser can be made practically identical to that of a diode laser by lessening the thickness of the sandwich layer.

| KEYWORDS

Quantum dots, quantum well, VLSI, quantum computing, Quantum Programming, biosensing

| ARTICLE INFORMATION

ACCEPTED: 11 December 2022 **PUBLISHED:** 20 December 2022 **DOI:** 10.32996/jcsts.2022.4.2.20

1. Introduction

Surface plasma wave SPW is a directed electromagnetic mode that spreads along the connection point between a conductor and a dielectric. Its field rots dramatically away from the connection point, the dielectric, as well as into the conductor. The rot is fast in the guide; consequently, the SPW field is confined in a meager skin layer. Inside the dielectric, the decay is less fast. An instance of extensive interest is the one where the dielectric is supplanted via air, and SPW spreads along the metal-air interface. The presence of little hints of material on the connection point gets a significant change in the engendering qualities of the SPW. Due to these qualities, the SPW is undeniably appropriate for biosensors and nanoparticle sensors.

Several energy-transfer processes may occur for dipoles near a metal-dielectric interface 40. Three processes involve SPP quanta for dipoles overlapping spectrally and with SPP electric fields: an exciting dipole spontaneously emits an SPP (Fig. B2a); a dipole in the ground state is excited by the absorption of an SPP (Fig. B2b), or an exciting dipole is stimulated to emit an SPP clone (Fig. B2c). Other processes involving excited dipoles include the spontaneous creation of electron-hole pairs in the metal through dipole-dipole coupling (for dipoles that are very close) (Fig. B2d) and the spontaneous emission of radiative modes (Fig. B2e). The excitation of radiative modes and electron-hole pairs in the metal corresponds to energy loss. Spontaneously emitted SPPs contribute to noise in an amplifier or oscillator application. Amplification requires the inversion of the gain medium such that stimulated SPPs to dominate over SPP absorption(Sarid, 1981).

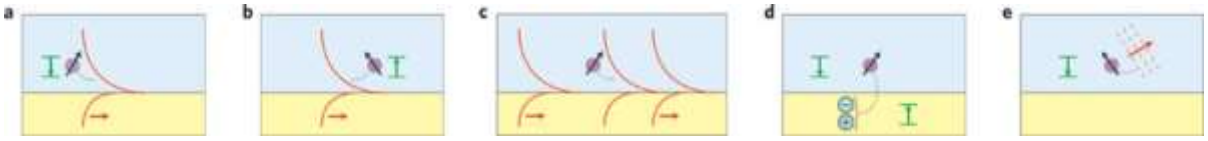

Optical processes occur for dipoles (purple) near a single metal-dielectric interface. The magnitude of the transverse electric field component of the SPP involved in the processes (red) is shown along with the associated dipole energy transitions (green). The dotted black curves indicate energy transfer. Spontaneous emission of SPPs. b, Absorption of SPPs. c, Stimulated emission of SPPs. d, Creation of electron-hole pairs. e, Spontaneous emission of radiation.

2. Dipoles near a metal-dielectric interface

2.1 LRSPP amplifier

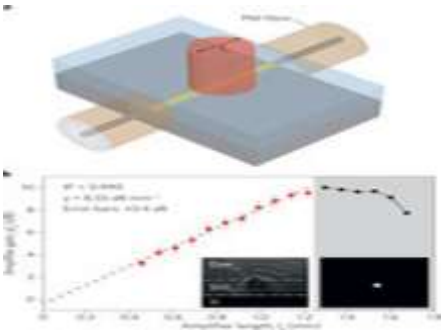

a LRSPP amplifier comprising a gold stripe on SiO2 (on silicon) covered by a dye gain medium (IR-140). The pump is polarized along the stripe length (Ep) and applied to the top of the structure. End-fire coupled input/output polarization-maintaining (PM) fibers are also shown. b, measured amplifier gain at a probe wavelength of λ = 882 nm versus amplifier length; the slope of the curve indicates the LPSPP mode power gain (γ = 8.55 dB mm–1).

PM-polarized light at = 633 nm was used to excite probe SPPs at the silver dye interface while the dye was excited at = 580 nm (~10 mW) by pump SPPs counter-propagating along the same interface (Fig.1a). For the 39-nm thick silver film, increased reflectance was noted over the SPP excitation. They measured an increase in reflectance at the SPP excitation angle due to the stimulated emission of SPPs and estimated an SPP loss reduction of 35% and a material gain of around 420 cm 1.

The prism during pumping in the absence of the probe and observed characteristics that they attributed to the amplified spontaneous emission of SPPs (ASE-SPPs). They pointed out that significant gain reduction may occur because of ASE-SPPs, and estimated a ~30% increase in SPP propagation length due to stimulated emission (Salama et al., 2019).

3. Methodology

The qualities of SPPs, and the wealthy wide range of metal components on which they are reinforced, mean that SPP amps and oscillators are unique from their traditional alternatives with regard to type and efficiency. The company of this Evaluation shows this diversity: performance on single-interface SPPs is protected first, followed by a performance on steel movies, steel clads, and versions thereof, and lastly, by performance on nanostructures. The incorporation of obtain with plasmonic metamaterials is also being intensely followed.

3.1 Single-interface SPPs

Prism and grating combining options are practical for interesting SPPs 1. The Kretschmann settings include a steel movie on the platform of a high-refractive-index prism, surrounded by a low-refractive-index method on the other part (Fig. 1c). A grating coupler presents a regular perturbation of corrugations, lumps on cuts to the steel. The part of the prism or grating is to improve the in-plane strength of TM-polarized occurrence mild such that it suits that of the SPP (Salama et al., 2019).

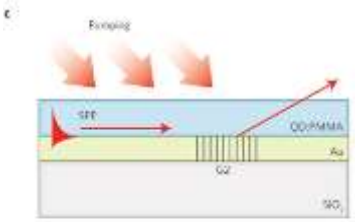

3.2 Long-range SPPs on symmetric metal films

Less material gain is required to amplify long-range SPSs calculated that the material gain required for lossless predicted that a material gain of 400 cm 1 was required for lossless 4,000 and threshold gains of around 200 cm 1 were predicted at = 1,400 nm for RRSP whispering gallery modes in metal GaAs the gain required for lossless propagation would be underestimated (Salama et al., 2019).

Supposing R6G in solution as the obtain method, lossless LRSPP reproduction at = 560 nm was expected under poor moving (= 532 nm, ~200 kW cm 2) of a moderate dye focus (N = 1.8 1018 cm 3) for a 20-nm-thick gold movie protected by the medium40 recommended that a grating assisting LRSPPs would function as a plasmatic band gap laser device if a obtain method whose optimum exhaust is within the bandgap is presented.

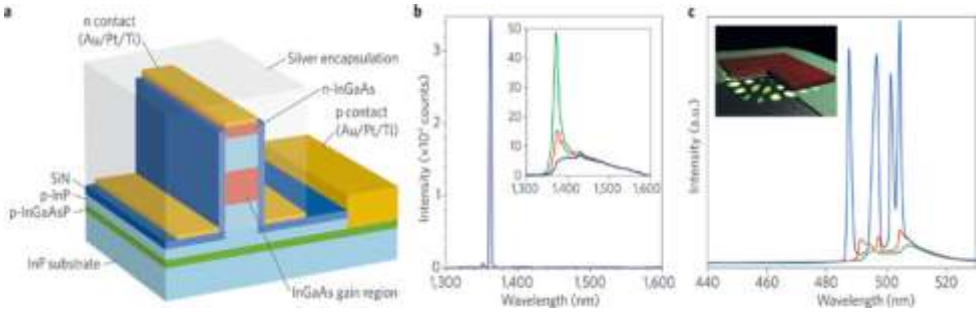

a. Fabry–Pérot metal-clad SPP laser comprising an Ag/SiN-coated rectangular InGaAs pillar; the thickness of the InGaAs gain region is 300 nm. b, Measured laser spectrum at 10 K for a 6-μm-long device biased at 200 μA; the width of the gain pillar is d = 90 nm and the thickness of the SiN layer is around 20 nm for a total width of approximately 130 nm. The inset shows emission spectra (also at 10 K) below the lasing threshold. c, Measured leakage spectra as a function of pump irradiance (black, 1,960 MW cm−2; red, 2,300 MW cm−2; blue, 3,074 MW cm−2). The inset shows an SPP cavity formed from a silver film covered by a 5-nm-thick layer of MgF2 and a square patch of CdS measuring 50 nm thick and 1 μm across.

3.3 SPPs in metal-clad waveguides

Symmetrical short-range SPPs (APPs) can be limited to very smaller portions in metal-gap53 and metal-clad 54 waveguides, which encourages their use for nano-amplifier and Nano laser programs. Although the attenuation of SRSPPs is great, theoretical research that semiconductors can offer enough obtain to make up for failures in some structures identified that content benefits in the variety of 1,625–4,830 cm–1 are needed for lossless SPP reproduction at λ = 1,500 nm for a gold-clad semiconductor movie calculating 50–500 nm in width. Acting an Au–InGaAs–Au framework, Chen et al.61 expected lossless SPP reproduction at λ = 1,550 nm for a content obtained of 2,500 cm–1 in a 75-nm-thick framework. They also examined the efficiency of a minoring laser device and expected a limit lasing present (density) of around 550 nA (1 kA cm–2). Remarkably, it is calculated that the obtained SPP near its power asymptote is much bigger than the content obtained from the method dressed by materials because the method's power speed is low in this area (Salama et al., 2019).

3.4 Other planar structures

A thin patterned dielectric layer on a metal film can act to confine or redirect SPPs63. Such structures, known as dielectric, loaded SPP (DLSPP) waveguides, have confinement and attenuation levels comparable to those of a SISPP. The dielectric layer is a natural host for dipolar emitters. Waveguides consisting of PMMA stripes (cross-section of 600 nm 400 nm) doped with PbS QDs on a 40-nm-thick gold film. The researchers conducted measurements of spontaneous and stimulated SPPs using Fourier-plane leakage radiation microscopy at 1,550 nm (near the QD emission peak) while pumping at = 532 nm. They measured the SPP propagation length as a function of pump intensity while probing at = 1,550 nm, observing a distinct threshold beyond which the propagation length increased linearly (up to 27% in this work) with the pump power. In subsequent work66, when investigating CdSe/ZnSe QD-doped PMMA stripes on a silver film, the researchers measured a comparable increase in propagation length at = 632.8 nm. reported a comparable (32%) increase in SPP propagation length in PbS QD-doped PMMA stripes on gold at 860 nm. By modelling DLSPP waveguides at wavelengths close to the SPP energy asymptote, it was found that nanoscale dielectric cross-sections of around 22 nm × 20 nm and dielectric gains of approximately 46,000 cm–1 would provide lossless subwavelength propagation at λ = 450 nm (Luque et al., 2012; Yamada et al., 2014).

3.5 Nanostructures

Small metal particles support resonant SPP modes that are characteristic of the particle's shape, size, and composition and also of the surrounding dielectric. The fundamental resonant mode of a metal nanosphere, for example, is dipolar, with densities of

opposing charge forming at opposite spherical caps. Resonances are excited by an applied laser field or nearby dipolar emitters. On resonance, the electric field in the vicinity of the particle is strongly enhanced (10–100 times) relative to the applied field (Salama et al., 2020).

3.6 Designer spoof surface plasmon structures collimate terahertz laser beams

Metamaterials and transformation optics offer major opportunities for the control of electromagnetic fields5, 6, 7, 8. The underlying paradigm is to design spatial variations of the magnitude and sign of the effective refractive index; thus, the optical path, or more generally the 'optical space', can be engineered in a continuous and almost arbitrary way. One can extend the concept to surface plasmon (SP) optics, where the dispersion properties of SPs are tailored by nanostructuring metallic surfaces with designer patterns. In this context, 'metasurfaces' or 'metafilms' have found interesting applications, such as subwavelength imaging9, waveguiding10,11 and the localization10, 11, confinement12 and slowing of light13 (Sohrabi et al., 2013).

Consider a structure composed of arrays of grooves with subwavelength periodicities textured on the surface of a plasmonic material (metals or highly doped semiconductors, which behave as metals in the terahertz regime; see Fig. 1a). Such a structure supports strongly confined surface waves with a dispersion relation ω(β) similar to SPs on a planar metal surface in the visible regime, as calculated by Pendry, Martín-Moreno, and García-Vidal3, 4 and observed on structured metals at terahertz frequencies14. The asymptotic frequency, ωspoof, is not solely determined by properties of the interface materials and can be designed over an extremely wide range by engineering the subwavelength pattern on the interface3 if the metal can be treated as a perfect electric conductor, ωspoof=πc/2h, where h is the groove depth, and c is the speed of light in vacuum4. Physically, this corresponds to first-order standing waves along the depth of the grooves. As ωspoof is primarily determined by surface texturing, one can engineer the spoof SP dispersion curve and obtain a sizeable deviation between the curve and the light line at terahertz frequencies; that is, β(ωTHz)>ko(ωTHz) (refs 3,4,14; see Fig. 1b). Here β is the in-plane wave vector of the SPs and ko is the free-space wave vector. As a result, the out-of-plane wave vector can be considerable, corresponding to confined SPs with a 1/e decay distance in the air normal to the interface equal to 1/|κ|.

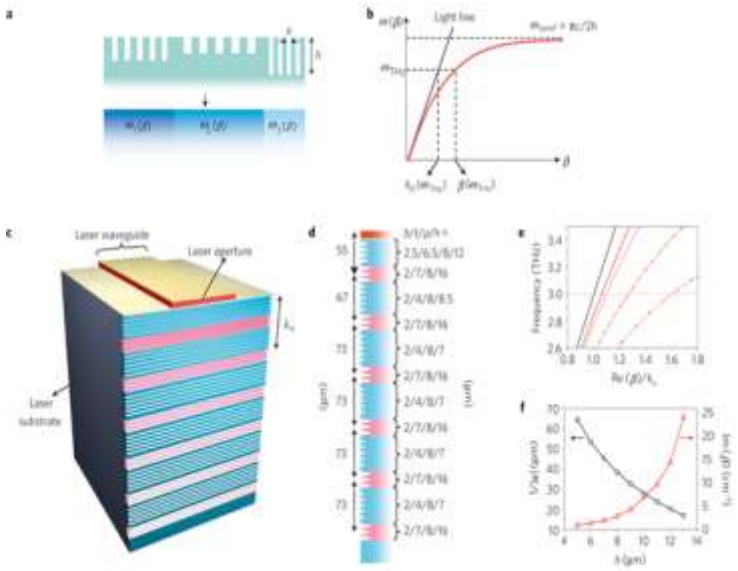

Terahertz plasmatic collimator design

4. Results and Discussion

Simulated distribution of the electric field (|E|) of the device. The simulation plane is perpendicular to the laser facet and along the plane of symmetry of the laser waveguide. b, Zoom-in view of a showing the region around the device facet. c,d, Simulated electric-field distribution (|E|) of a device with a conventional second-order grating (c) and of the original device (d). The conventional second-order grating was optimized to give the highest directivity, although it is still less effective than the spoof SP collimator. The centre-to-centre distance between the aperture and the closest groove of the second-order grating is 65 µm. The grating period is 88 µm. The opening, bottom, and depth of the second-order grating grooves are 19, 15, and 13.5 µm, respectively. e, The red, blue, and black curves are line-scans of the near-field (|E|) along and 10 µm above the facet for the devices in a, c and d, respectively. f, The red, blue, and black curves are calculated vertical far-field intensity profiles (|E|2) for a, c and d, respectively. Gaussian fits to the central lobes of the blue and red curves are plotted, and the area under the fits is shaded light blue and light

red, respectively. The shaded area is a measure of the percentage of total optical power in the main lobe. The main lobe of the device with the terahertz spoof SP collimator contains 70% of the output power, whereas it contains only 45% for the device with the second-order grating.

The QCL material was grown by molecular beam epitaxy on an undoped GaAs substrate. The growth sequence started with a 250-nm-thick undoped GaAs buffer layer and was followed by a 300-nm-thick Al0.5Ga0.5As etch-stop layer, a 75-nm-thick layer of GaAs n-doped to 5×1018 cm−3, the active region and finally a 50-nm-thick GaAs layer n-doped to 5×1018 cm−3. The active region consists of 170 periods of a two-phonon-resonance active region design similar to that of ref. 36, with a doping sheet density of ns=3.65×1010 cm−2. The material was processed into copper–copper waveguides using the following procedure19. First, a square centimeter of QCL material was cleaved and sputter-coated with Ta/Cu/Au (15/500/500 nm). The material was then wafer-bonded to a highly doped (1.6×1018 cm−3) GaAs substrate coated with sputtered layers of Ti/Au(15/500 nm). The bonded QCL wafer was next polished and wet-etched down to the etch-stop layer with a hydrogen peroxide/ammonium hydroxide solution (19:1 in volume), and the etch-stop layer was stripped with concentrated hydrofluoric acid. The laser ridges, with widths ranging from 25 to 150 μm, were then defined using dry etching with a SU-8 2005 photoresist mask. After SU-8 removal, metal (Ta/Cu/Au, 15/100/30 nm) was sputtered on top of the laser ridges. A gold capping layer was added to the waveguides with copper cladding to avoid copper oxidation and facilitate wire bonding. The processed wafers were finally cleaved into 1–2-mm-long bars and indium-mounted onto copper blocks (Salama et al., 2021).

The highly doped semiconductor substrate supports surface waves in the terahertz spectral range. We used the Dude model to calculate the dielectric permittivity of highly doped GaAs at terahertz frequencies40, 41 and found that the real part of the permittivity is negative. For example, ϵGaAs∼−200+42i for our device and measurement conditions (λo=100 μm, GaAs n-doped to 1.6×1018 cm−3, T=80 K). The propagation distance of surface waves (defined as the 1/e decay length of the electric field) along a planar GaAs/air interface under these conditions corresponds to ∼3 cm (∼300λo), which is about 10% of that of surface waves on a planar gold surface. Therefore, the highly doped GaAs function like a poor metal at terahertz frequencies, which is unlike the situation for visible and near-infrared wavelengths. It is extremely beneficial that metals are not needed for plasmonic in the terahertz regime because this greatly simplifies device fabrication (Sugaya et al., 2011).

In our system (surface-corrugated GaAs n-doped to 1.6×1018 cm−3 at T=80 K), the determination of the asymptotic frequency of the spoof SP dispersion curve is quite complicated because it involves three factors: the subwavelength pattern, the free-carrier concentration and the restorable band of GaAs. If one assumes that the spoof SP pattern is defined in a perfect electric conductor, the asymptotic frequency will ∼30–67 THz for the groove geometries used(Likharev, 1999). However, it will be further lowered considering the actual dielectric permittivity of GaAs, which is affected by the free-carrier concentration and the restorable band of GaAs. On the one hand, the Dude model predicts that the free-carrier concentration can support 'metallic' GaAs (that is, the real part of the permittivity <0) up to ∼10 THz. On the other hand, the restorable band of GaAs (∼7.5–10 THz; ref. 42) is going to introduce a large negative permittivity when an electromagnetic field strongly interacts with the optical phonons. The actual asymptotic frequency is, therefore, ∼7.5 THz, primarily determined by the restorable band of GaAs.

All devices were tested in pulsed mode with 60-ns pulses at 0.3% duty cycle (60-ns pulses at a 100 kHz repetition rate, with an extra 1 kHz modulation at 50% duty cycle for lock-in detection). Laser powers were measured using a Fourier transform infrared (FTIR) spectrometer with a calibrated helium-cooled bolometer using two 2′′-diameter parabolic mirrors: one with a 5 cm focal length to pass light from the devices to the input of the FTIR spectrometer and the other with a 15 cm focal length to focus the light from the output of the FTIR spectrometer onto the bolometer. To map the 2D far-field emission profile of the devices, a cryostat, in which the lasers were mounted vertically (laser material layers normal to the horizontal plane), was placed on a rotation stage. Line-scans of the laser far-field along the θ direction were obtained as the stage was rotated in the horizontal plane. The relative height of the cryostat and the bolometer was adjusted to allow many line-scans of the device far-field to be obtained and finally constructed into a 2D map(Gudlavalleti et al., 2021).

Quantum-cascade laser operating wavelengths are reported. The wavelengths were chosen in order to avoid major phonon absorption bands, which are particularly strong at energies just above the reststrahlen band (Sohrabi et al., 2013; Yoshida et al., 2010).

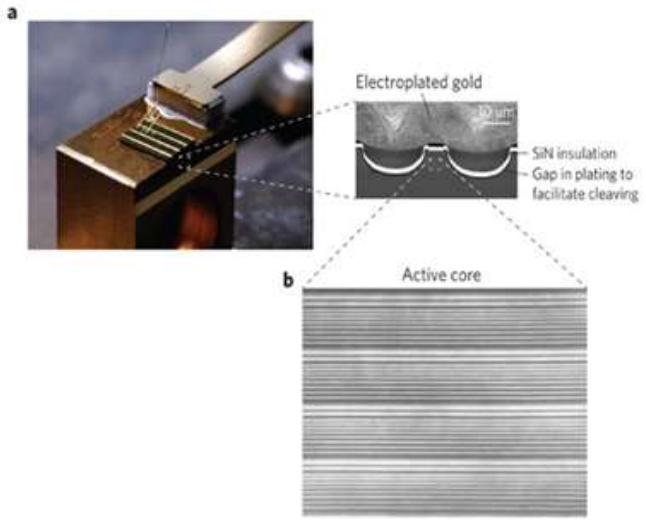

A, Photograph of a laser bar with four QC lasers (left, courtesy of Frank Wojciechowski) and scanning electron microscopy image of the front facet of a QC laser (right). **b**, High-resolution transmission electron microscopy image of a QC laser, showing four periods of active regions and injectors (Tayagaki et al., 2013).

5. Conclusion

Optical dipoles can be incorporated into dielectrics (such as polymers and glasses) and conveniently integrated with metal SPP structures (Salama & Youssef, 2018; Zhang et al., 2022). Although the solubility limit of dyes may be very high, the concentrations used in practice are far lower because of concentration-dependent effects that limit the excited state population density (such as Forster energy transfer between dipoles) or reduce the quantum efficiency and lifetime of the dipoles (such as the formation of dimers or clusters). Metal features can also be damaged by the pump: one value for the ablation threshold of bulk silver. Although suitable for some applications, optical pumping may be inconvenient, and strong optical pumping generates heat and causes damage. Electrical pumping is more convenient than optical pumping but is essentially limited to semiconductors. The energy efficiency of SPP amplification and lasing must be improved, although gain reduction close to the metal due to dipole quenching may place stringent limits on QD solar cells that are not far from being realized.

Funding: This research received no external funding.

Conflicts of Interest: The authors declare no conflict of interest.

Publisher's Note: All claims expressed in this article are solely those of the authors and do not necessarily represent those of their affiliated organizations, or those of the publisher, the editors and the reviewers.

References

[1] Gudlavalleti, R. H., Saman, B., Mays, R., Salama, H., Heller, E., Chandy, J., & Jain, F. (2021). A Novel Addressing Circuit for SWS-FET Based Multivalued Dynamic Random-Access Memory Array. *29*(1–4). https://doi.org/10.1142/S0129156420400091

[2] Likharev, K. K. (1999). Single-electron devices and their applications. *Proceedings of the IEEE*, *87*(4), 606–632. https://doi.org/10.1109/5.752518

[3] Luque, A., Martí, A., & Stanley, C. (2012). Understanding intermediate-band solar cells. *Nature Photonics 2012 6:3*, *6*(3), 146–152. https://doi.org/10.1038/nphoton.2012.1

[4] Salama, H., Saman, B., Gudlavalleti, R. H., Chan, P. Y., Mays, R., Khan, B., Heller, E., Chandy, J., & Jain, F. (2020). Simulation of Stacked Quantum Dot Channels SWS-FET Using Multi-FET ABM Modeling, *28*(3–4). https://doi.org/10.1142/S0129156419400251

[5] Salama, H., Saman, B., Gudlavalleti, R., Mays, R., Heller, E., Chandy, J., & Jain, F. (2021). Compact 1-Bit Full Adder and 2-Bit SRAMs Using n-SWS-FETs. *29*(1–4). https://doi.org/10.1142/S0129156420400133

[6] Salama, H., Saman, B., Heller, E., Gudlavalleti, R. H., Mays, R., & Jain, F. (2019). Twin Drain Quantum Well/Quantum Dot Channel Spatial Wave-Function Switched (SWS) FETs for Multi-Valued Logic and Compact DRAMs. *Https://Doi.Org/10.1142/S0129156418400244*, *27*(3–4). https://doi.org/10.1142/S0129156418400244

[7] Salama, H., & Youssef, T. (2018). VOLTAGE STABILITY OF TRANSMISSION. *International Journal of Innovation and Applied Studies*, *24*(2), 439–445.

[8] Sarid, D. (1981). Long-Range Surface-Plasma Waves on Very Thin Metal Films. *Physical Review Letters*, *47*(26), 1927. https://doi.org/10.1103/PhysRevLett.47.1927

[9] Sohrabi, F., Nikniazi, A., & and, H. M. (2013). Optimization of third-generation nanostructured silicon-based solar cells. *Solar Cells—Research and Application Perspectives; Morales-Acevedo, A.*

[10] Sugaya, T., Numakami, O., Furue, S., Komaki, H., Amano, T., Matsubara, K., Okano, Y., & Niki, S. (2011). Tunnel current through a miniband in InGaAs quantum dot superlattice solar cells. *Solar Energy Materials and Solar Cells*, *95*(10), 2920–2923.

https://doi.org/10.1016/J.SOLMAT.2011.06.034
[11] Tayagaki, T., Hoshi, Y., & Usami, N. (2013). Investigation of the open-circuit voltage in solar cells doped with quantum dots. *Scientific Reports 2013 3:1*, *3*(1), 1–5. https://doi.org/10.1038/srep02703
[12] Yamada, S., Kurokawa, Y., Miyajima, S., & Konagai, M. (2014). Silicon quantum dot superlattice solar cell structure including silicon nanocrystals in a photogeneration layer. *Nanoscale Research Letters*, *9*(1), 1–7. https://doi.org/10.1186/1556-276X-9-246/FIGURES/7
[13] Yoshida, K., Okada, Y., & Sano, N. (2010). Self-consistent simulation of intermediate band solar cells: Effect of occupation rates on device characteristics. *Applied Physics Letters*, *97*(13), 133503. https://doi.org/10.1063/1.3488815
[14] Zhang, L., Fakhrabadi, R. D., Khoshkhoo, M., & Salama, H. (2022). *A Robust Second-Order Conic Programming Model with an Effective Budget of Uncertainty in Optimal Power Flow Problem*. https://doi.org/10.20944/PREPRINTS202203.0384.V1